Published in final edited form as:
Lab Chip. 2008 January ; 8(1): 88–97. doi:10.1039/b711770a.

Microfabricated Valveless Devices for Thermal Bioreactions based on Diffusion-limited Evaporation

Fang Wang[a,†], **Ming Yang**[a,†], and **Mark A. Burns**[a,b,*]

[a] Department of Chemical Engineering, University of Michigan, Ann Arbor, MI 48109

[b] Department of Biomedical Engineering, University of Michigan, Ann Arbor, MI 48109

Abstract

Microfluidic devices that reduce evaporative loss during thermal bioreactions such as PCR without microvalves have been developed by relying on the principle of diffusion-limited evaporation. Both theoretical and experimental results demonstrate that the sample evaporative loss can be reduced by more than 20 times using long narrow diffusion channels on both sides of the reaction region. In order to further suppress the evaporation, the driving force for liquid evaporation is reduced by two additional techniques: decreasing the interfacial temperature using thermal isolation and reducing the vapor concentration gradient by replenishing water vapor in the diffusion channels. Both thermal isolation and vapor replenishment techniques can limit the sample evaporative loss to approximately 1% of the reaction content.

Introduction

Many reactions used for biochemical analysis are temperature-controlled and require relative high operating temperatures. One of the most well known thermal reactions is the polymerase chain reaction (PCR), an enzyme-catalyzed DNA amplification cycles through three different temperatures (denaturation (~94°C), annealing (~55°C) and extension (~72°C)). Sanger cycle sequencing is another thermocycling reaction (~95°C, ~55°C, ~60°C) that utilizes the termination function of dideoxynucleotide triphosphates (ddNTPs) on DNA chain enlongation. [1] Ligase chain reaction (LCR) and ligase detection reaction (LDR), techniques used to detect single base mutations, both require elevated temperatures. [2] Restriction of DNA strands into shorter fragments for DNA analysis is an isothermal reaction but still requires temperatures up to ~75°C. Traditionally, these biochemical assays have been carried out in bench-top equipment (*e.g.*, themocyclers) and, although there are many potential applications, the techniques have not been widely disseminated, particularly for point-of-care applications.

In recent years, microfabrication technologies have paved the way for the development of rapid and inexpensive bioreaction systems. A miniaturized bioreaction system presents several advantages over the bench-top equivalent: reduced reagent, labor and equipment costs, decreased reaction time, reduced risk of contamination, and simplified sample handling. There are two major types of miniaturized bioreaction systems: batch-based systems where the stationary reaction solution is heated or thermocycled inside a reaction chamber by either external heaters [3–16] or integrated on-chip heaters, [17–24] and continuous flow-based systems where the sample flows through certain temperature zones with well-defined flow rates. [25–30] Other novel approaches, such as on-chip rotary reaction, [31] noncontact infrared-mediated

*Email: maburns@umich.edu; Fax: (734) 763 0459; Phone: (734) 764 4315.
†These authors contributed equally to this work.

reaction, [32–34] electrokinetically synchronized reaction, [35] electrowetting-based reaction [36] and Rayleigh-Bénard convection-based reaction [37,38] have also been reported. Recent trends in miniaturized bioreaction systems are to integrate bioreactions with sample preparation, fluidic handling, and product detection to produce systems that can rapidly, conveniently, and economically extract information from raw biological samples with greatly reduced cost. [4,7,11,12,17–20,23,39]

One technical challenge in miniaturizing bioreaction systems is preventing or reducing evaporative loss during thermocycling. Although mineral oils, [4–16,10,26] adhesive tapes [19,22] and silicone rubber gaskets [21] have all been used in miniaturized bioreaction devices, most integrated systems reported so far have used microvalves to prevent evaporative loss. These microvalves seal the reaction chamber using pneumatically or mechanically actuated diaphragms, [7–9,11,15,17–18,40–43] thermally actuated phase-change pistons, [12,19,39,44] or polyacrylamide gels.[19] Because all microvalves need to provide some kind of physical confinement and most require some kind of actuations to operate, they often add complexity to the microfabrication and fluidic operations. In addition, simple microfluidic assays are often open or unsealed systems to allow the introduction and/or the withdrawal of fluids. Therefore, a simple technique to reduce the evaporative loss without valves is highly desirable for microfluidic reaction systems.

We have fabricated microfluidic devices that use diffusion-limited evaporation mechanisms to suppress liquid loss during thermal reactions. Eliminating the use of microvalves, oil or gaskets, the basic design uses long narrow diffusion channels in the fluidic network to slow down the diffusion of water vapor through the channel openings. The vapor evaporation rate can be further reduced by decreasing the driving force for liquid evaporation. This reduction is achieved either by decreasing the sample interfacial pressure using thermal isolation or by decreasing the vapor concentration gradient using vapor replenishment.

Theory and design principles

The principle of valveless reaction devices is based on the concept of diffusionlimited evaporation. In the design, the input and output channels to the heated reaction chamber provide a resistance that decreases the evaporation rate from the reaction fluid (see Figure 1(a)). Vapor that evaporates from the reaction solution meniscus must diffuse through the microchannels before it can escape through sample loading holes into the ambient environment. The evaporation rate is limited by this vapor diffusion rate since the phase change at the liquid surface (*i.e.*, liquid to vapor) is quite rapid and there is no convective flow of air in the channel.

The diffusion-limited evaporation rate can be evaluated using mass transfer equations. At any given time, there is a vapor-pressure gradient along the diffusion path, from the equilibrium interfacial vapor pressure at the liquid meniscus to the ambient vapor pressure at the outlets. As evaporation proceeds, the sample interface recedes in the channel, resulting in an increased diffusion length over time. According to Fick's law, the total diffusion flux of vapor N_A in the channel (in the x direction) is determined by

$$N_A = -\frac{PD_v}{RT(1-y)}\frac{dy}{dx}, \tag{1}$$

where P is the total pressure; y is the mole fraction of vapor ($y=\frac{p_A}{P}$ and p_A is the partial vapor pressure); D_v is vapor diffusivity in air; T is liquid interfacial temperature; and R is the ideal

gas constant. Integrating equation (1), we obtain the total diffusion flux of vapor at any given moment,

$$N_A = \frac{PD_v}{RTx} \ln \frac{P - p_v}{P - p_0}, \tag{2}$$

where x is the diffusion length (*i.e.*, the distance between the sample interface and the loading holes); p_0 and p_v are the ambient and sample interfacial vapor pressures, respectively. Assuming a pseudo-steady-state condition (*i.e.*, the sample interface recedes slowly), the diffusion flux also equals the amount of water leaving the liquid meniscus,

$$N_A = \frac{\rho_w}{M_w} \frac{dx}{dt}, \tag{3}$$

where M_w and ρ_w are the molecular weight and density of water, respectively. Combining equation (2) and (3), and integrating from $t = 0$ to $t = t_F$, we obtain the distance from the sample interface to the sample access hole as a function of time at a constant temperature:

$$x_F^2 - x_0^2 = \frac{2PM_w D_v t_F}{\rho_w RT_i} \ln\left(\frac{P - p_0}{P - p_v}\right), \tag{4}$$

where x_0, x_F are the initial and final diffusion lengths, respectively; T_i is sample interfacial temperature; and t_F is the reaction time.

For a thermocycling reaction, equation (4) must be modified to include periodically changed sample interfacial temperatures, T_i, and reaction time, t_F. The vapor pressure, p_v, and vapor diffusivity, D_v, also need to be changed periodically because they are temperature dependent.[45,46] For example, three sets of T_i, p_v, t_F and D_v are needed for PCR that consists of three-step thermocycling. The total evaporative volume loss during a three-step thermocycling reaction, $V_{loss,}$ is then calculated using equation (5),

$$V_{loss} = 2A_c(x_F - x_0) = 2A_c\left(\sqrt{n\sum_{j=1}^{3}\frac{2PM_w D_{vj} t_{Fj}}{\rho_w RT_{ij}} \ln\left(\frac{P - p_0}{P - p_{vj}}\right) + x_0^2} - x_0\right), \tag{5}$$

where T_{ij}, p_{vj}, t_{Fj} and D_{vj} are the sample interfacial temperature, vapor pressure, reaction time and vapor diffusivity at different thermocycling steps, respectively; n is the number of cycles; and A_c is the cross-section area of the diffusion channel. In this equation, variables such as t_{Fj}, n, M_w and ρ_w are determined by the reaction protocols, and p_0 is negligible compared to the atmosphere pressure P. Therefore, the variables that we can adjust to reduce V_{loss} in the microfabricated devices are the initial diffusion length x_0 that is associated with the channel length L, the channel cross-section area A_c, and the sample interfacial temperature T_{ij}. The temperature near the sample interface also determines the interfacial vapor pressure p_{vj} and the vapor diffusivity D_{vj}.

Materials and methods

Device design and fabrication

The long-armed device with thermal isolation contains a 4mm long, 2mm wide and 100μm deep reaction chamber with a rough volume of 800nL, and two 1cm long, 200μm wide and 20μm deep channels connected to the reaction chamber. The reaction chamber is surrounded by a 1μm thick and 1mm wide silicon nitride diaphragm. The device with vapor replenishment consists of a serpentine reaction channel (designed volume of 500nL) with two 5mm long and 100μm wide straight channels on either end. All channels in this device are 50μm deep except that there are two 150μm deep liquid stop structures near the T-junctions in the water channels.

The devices are assembled by bonding silicon and glass substrate components. The fluid networks are fabricated in a glass wafer using two photolithography and two-step wet chemical etching due to the non-uniform depth. The detailed procedure for photolithography and wet etching have been outlined elsewhere.[32] In the fabrication process of the thermally isolated long-armed device, the first lithography is carried out to only pattern the deeper features (*i.e.*, the reaction chamber), followed by etching away the exposed metal film. The remaining photoresist is then stripped away. The second lithography is carried out to pattern the whole fluid network. The glass wafer is then etched to generate the reaction chamber with a depth of 80μm in hydrofluoric acid (49%, CMOS grade; J.T. Baker, Philipsburg, NJ). After removing the metal film that protects the channels, the second glass etching is conducted to an additional depth of 20μm. Then the remaining photoresist and metal film are removed. The fabrication of fluid network in the vapor-replenished device follows a similar procedure, except that the etching depth in each etching step is different according to the design. Sample access holes are drilled by a homemade electrochemical discharge drilling system. Finally, the glass wafer is coated with 5μm parylene in a parylene coating system (PDS-2010 LABCOTER®2, SCS Cookson Electronics, Indianapolis, IN), and diced to yield the individual devices.

Silicon fabrication process of the vapor-replenished device is the same as described in previous work.[38] Silicon fabrication of the thermally isolated long-armed device begins with depositing a 1μm thick low stress silicon nitride on a silicon wafer (<100>, 500μm thick) by low pressure chemical vapor deposition (LPCVD). The lithography and liftoff for the heaters and sensors have also been described in previous work.[38] To thermally isolate the reaction chamber, another lithography is carried out on the backside of the silicon wafer. The exposed silicon nitride layer is then removed by CF_4/CHF_3 plasma RIE process. Next, a deep reactive ion etching (DRIE) process is carried out to selectively remove the silicon substrate and thus obtain a 1μm thick silicon nitride diaphragm.

The procedure to assemble the glass-silicon device has also been described in detail elsewhere.[38] Briefly, Individual silicon devices are fixed on the custom designed printed circuit board (PCB, Advanced Circuits, Aurora, CO), and then wire bonded (Kulicke & Soffa 4124 Ball Bonder) using 1.0 mil gold wire. Next, the assembly is coated with 5μm parylene. The silicon and glass components are visually aligned and then bonded using UV curable optical glue. Finally, the wirebonds are encapsulated with a non-fluorescent epoxy (EP939; Thermoset, Indianapolis, IN).

Instrumentation

The setup for reaction temperature control consists of a DC power supply (B+K Precision Model 1760, Yorba Linda, CA), two data acquisition (DAQ) boards (National instruments PCI 6031E and PCI-6704, Austin, TX), two connector blocks (National instruments SCB-100 and SCB-68, Austin, TX), a signal conditioning circuit, a computer and two LabVIEW programs (National instruments, Austin, TX). The temperature sensors are calibrated by heating the

device in a convection oven and recording the temperature-resistance data in a LabVIEW program. The slope and intercept from a linear fit of the temperature and resistance data is read into the control algorithms that use a proportional-integral (PI) module to control temperature. The heaters are connected to the power supply through the signal conditioning circuit that boosts the supply voltage from the computer with an op-amp gain of 3. During the experiments, the device is placed on a copper block that sits on a probe station chuck at room temperature. Lab air supply, controlled by a pressure regulator (Matheson Gas Products Inc, Irving, TX, Model Number 3701), provides the pneumatic pressure used for fluidic operations.

PCR amplification and analysis

PCR amplification of the Influenza viral strain A/LA/1/87 DNA samples is performed on the devices. The hemaggultinin gene (HA1) region of influenza viral RNA is reverse transcribed, amplified, ligated into pGEM-T vector, and cloned into *E. coli*. The cloned plasmid is used to synthesize RNA *in vitro* with T7 RNA polymerase. The RNA samples are then subject to reverse transcription to produce the DNA samples that are used in the device. The reaction mixture consists of 2ng/μL DNA template, 0.2mM each dNTP, 60mM Tris-HCl, 15mM NH_4SO_4, 1.5mM $MgCl_2$, 0.3mM each primer, and Taq DNA polymerase 50units/mL (Invitrogen, Carlsbad, CA). The sequences of forward and reverse primers are 5′-GTTTGTTTCTCTGGTACATTCCGC-3′ and 5′-CAACTGTTACCCTTATGATGTGCC-3′, respectively. A DNA fragment of 690bp is amplified. The thermocycling protocol used by the on-chip PCR consists of 30 cycles of 94°C for 5s, 55°C for 10s, 72°C for 20s, and 72°C for 30s after 30 cycles. The reaction solution is then collected and analyzed on a 1% agarose gel electrophoresis prestained with ethidium bromide.

Results and discussions

Based on the principle of diffusion-limited evaporation, three approaches are proposed to reduce the sample evaporative loss in a microfluidic device during thermal reactions. First, long channels with small cross sections at both ends of a reaction chamber increase the diffusion path of the evaporated vapor, greatly reducing the vapor diffusion rate. Second, a thin silicon nitride diaphragm surrounding a reaction chamber thermally isolates the high-temperature reaction region from the rest of the device, significantly lowering the temperature and vapor pressure at the liquid interface as well as the driving force for evaporation. Third, a pure water meniscus, pinned at the edge of a deep pit that connects to the diffusion channel, is heated synchronously with the reaction chamber to increase the vapor concentration in the diffusion channel and therefore decrease the concentration gradient (*i.e.*, the driving force for evaporation). Each of these techniques is described in the following sections.

Diffusion channel geometry and initial diffusion length

For thermal reactions in microfluidic systems such as PCR, evaporative loss can be significant compared to the reaction volume if valves or seals are not used. Figure 1(b) shows the evaporative loss (V_{loss}) during thermocycling as a function of the amount of liquid that is initially present in the reactor. For these experiments, we used a simple 13 reactor design consisting of a straight channel with uniform cross-section area (Figure 1(a)). The evaporative loss is measured by heating the entire channel using the PCR protocol mentioned previously. As shown in Figure 1(b), the evaporative loss (V_{loss}) in a straight uniform channel during thermocycling (30 cycles of 94°C for 5s, 55°C for 10s, 72°C for 20s) is approximately 40% ~100% of the original reaction volume (V_{PCR}).

Using equation (5), we also calculated the relative sample evaporative loss (V_{loss}/V_{PCR}) in a uniform channel with different channel lengths (L) and initial diffusion lengths (x_0) when the channel is thermocycled. The temperatures used in the cycling, and the vapor pressure and

diffusivity at different temperatures are listed in Table 1. The results in Figure 1(c) show that with the same fractional filled length ($(L-2x_0)/L$), the evaporative loss is reduced dramatically by increasing the channel length (*i.e.*, the length of the diffusion regions). For a certain percentage of sample evaporative loss, the optimal initial diffusion length and the minimal channel length can be determined using Figure 1(c). For example, to keep the evaporative loss to no more than 10%, the channel should be at least 4cm long with a fractional filled length of 0.5 (*i.e.*, x_0=1cm on both ends). The plot also indicates that in most cases, designing the channel so that the reaction solution fills it half way ($(L-2x_0)/L = 0.5$) will result in less relative evaporative loss than if the channel is filled completely ($(L-2x_0)/L =1$) or hardly at all ($(L-2x_0)/L \leq 0.1$). In fact, although the absolute value of evaporative loss is very small when the channel is almost empty, V_{loss}/V_{PCR} is still large due to the small initial reaction volume.

In addition to the channel length and initial diffusion length, the cross-section area of the channel also affects the V_{loss}/V_{PCR} ratio as predicted in Figure 1(d). In this calculation using equation (5), we divide the channel into three regions: a reaction region with the cross-section area A_r, and two diffusion regions on either end of the reaction region with the cross-section area A_c. The results show that the smaller the value of A_c/A_r is, the less the evaporative loss will be, implying that narrow diffusion channels with large reaction chambers are preferred. Note that actual evaporation rates may increase in narrow channels due to the increased extent of liquid film wetting on the channel wall.[48]

Driving force for liquid evaporation

Thermal isolation—In addition to controlling the design geometry, the evaporative loss can be further reduced by reducing the liquid interfacial temperature using thermal isolation. As is known, the driving force for liquid evaporation is the difference between the interfacial vapor pressure p_v and the ambient vapor pressure p_0. p_v is strongly associated with the interfacial temperature T_i, and thus decreasing T_i will decrease p_v and the driving force for liquid evaporation. In order to obtain low interfacial temperature, excellent thermal isolation is required because in most microfabricated reactors the low temperature region at the sample interface is very close to the high temperature region in the reaction chamber. Similar to what has been demonstrated previously, [47] a low stress silicon nitride diaphragm surrounding the reaction chamber can be used to produce good thermal isolation characteristics, resulting in a lower sample interfacial temperature that helps to suppress evaporation (Figure 2).

The interfacial temperature, T_i, during a thermal bioreaction is predicted using steady-state heat transfer simulations. Both devices that we simulated contain a long-armed chamber (*i.e.*, a large reaction chamber with two long narrow channels on both ends). In addition, the chamber in one device is thermally isolated with a thin diaphragm as depicted in Figure 2(a) (also see Figure 1 in ESI). As was demonstrated before, [47] the temperature throughout the device without thermal isolation is significantly higher than with thermal isolation (see Figure 1 in ESI). This temperature difference is mostly due to a more than three orders of magnitude difference in the thermal conductivities of silicon and air (150 W/m·K *vs.* 0.026 W/m·K).

To investigate the evaporative loss in a long-armed device with thermal isolation, the relative evaporative loss (V_{loss}/V_{PCR}) is calculated theoretically and experimentally. The theoretical V_{loss}/V_{PCR} ratios are calculated using equation (5) and the simulation results of interfacial temperature (listed in Table 1). The experimental V_{loss}/V_{PCR} ratios are measured during the reaction in a long-armed device with and without thermal isolation. Both theoretical and experimental V_{loss}/V_{PCR} ratios are plotted in Figure 3(a). The plot indicates that the experimental data fit fairly well with the theoretical results, and that the thermally isolated device significantly reduces the evaporative loss compared to the device without thermal isolation. In most cases, with $(L-2x_0)/L < 0.83$ (*i.e.*, $x_0 > 2mm$), the evaporative loss in the

device without thermal isolation is more than 5 folds higher than that in the thermally isolated device.

The gel electrophoresis of PCR products collected from the thermally isolated devices shows that most on-chip PCR exhibits similar amplification efficiency to the off-chip positive control (Figure 3(b)). No byproduct bands have been detected from both on-chip and off-chip PCR and the yield (brightness analysis) of amplification increases with the reduction of the evaporative loss. This result is understandable since evaporative loss changes not only the reaction volume, but also the sample and reagent concentrations. However, amplification from different template DNAs requires different optimal concentration and thermocycling conditions. Thus, the effect of reducing the evaporative loss on the PCR yield may vary for other DNA samples.

A potential problem associated with this thermal isolation device is that part of the reaction solution (*i.e.*, the sample in the long narrow channels) will not be amplified because it does not experience the desired thermocycling temperatures. However, the results in Figure 3(b) indicate that the unreacted sample volume in the channels will not significantly affect the overall PCR fidelity and efficiency because the narrow channels have limited volume of extra solution (less than 10% of the total reaction volume).

To facilitate the reduction of evaporative loss while assuring the reaction efficiency, some key design factors need to be optimized. The width of the silicon nitride diaphragm is one factor that can significantly affect the interfacial temperature. As shown in Figure 4(a), a wider diaphragm is expected to provide better thermal isolation and further reduce the evaporative loss. This improvement, however, becomes negligible when the diaphragm is wider than 1.5mm. In addition, larger diaphragms may require longer fabrication time and are sometimes more difficult to handle, implying an optimal width between 1mm and 1.5mm. According to the previous discussions, complete removal of the silicon under the reaction chamber will provide better thermal isolation because it further reduces the heat conduction between the chamber and the rest part of the device.[47] However, heat transfer simulations reveal that in such a design the temperature uniformity in the reaction chamber will be poor compared to the current design in which the chamber is supported by silicon (see Figure 2 in ESI).

The reaction volume also plays an important role in designing long-armed devices with thermal isolation. The result in Figure 4(b) indicates that the difference of evaporative loss in a long-armed device with and without thermal isolation is much more prominent for a smaller reaction volume (or smaller cross-section area of reaction chamber). In the current design with a relatively large reaction volume (~800nL), even a device containing long diffusion channels without thermal isolation can reduce the evaporative loss to less than 4%. However, if the reaction chamber volume is reduced to 100nL, the evaporative loss is 20% when $(L - 2x_0)/L = 0.83$ (*i.e.*, $x_0 = 2mm$) in the device without thermal isolation, while only 4% in a thermally isolated device. Therefore, it is more advantageous to use a thermally isolated device for small volume reactions.

Vapor replenishment—The driving force for liquid evaporation (*i.e.*, the water vapor concentration gradient) can also be reduced using vapor replenishment. Vapor generated at a pinned water meniscus on both sides of the reaction channel can be used to offset vapor lost from the reaction volume (Figure 5(a)). This pinned meniscus increases the water vapor concentration near the reaction solution meniscus, thus reducing the vapor concentration gradient in the channel. The key feature in this design is the liquid stop fabricated by etching a deep pit near the T-junction (Figure 5(b)). The principle of liquid stop is based on the surface energy change when the cross-section of capillary enlarges abruptly.[49] The liquid stop not only

prevents the mixing of the reaction solution with the water reservoirs during fluidic operation, but also defines the location of the water meniscus and thus the vapor source.

Steady-state mass transfer simulations confirm the reduction of water vapor concentration gradient and flux in the diffusion channels using vapor replenishment. The results of concentration and flux values along the centerline of the diffusion channel when the reaction solution is at 94°C are plotted in Figure 6(a) and 6(b). Without vapor replenishment, the vapor concentration decreases from the reaction solution meniscus ($x = 5mm$) to the sample access hole ($x = 0mm$) (Figure 6(a)), while the total vapor flux is constant along the channel (Figure 6(b)). The results in Figure 6(a) also indicate that adding vapor into the diffusion channel reduces the vapor concentration gradient between the liquid stop and the reaction solution meniscus and thus the driving force for liquid evaporation. Clearly the vapor replenishment increases the total vapor flux from the liquid stop to the sample access hole ($0<x<2.5mm$), but decreases the flux from the reaction volume ($2.5mm < x < 5mm$) in comparison to a constant flux in a straight channel design (Figure 6(b)).

Both simulation and experimental results demonstrate that the operating temperatures at the pinned water meniscus significantly affect the water vapor flux, as shown in Figure 6(c). In fact, when the operating temperature is higher than 95°C and the reaction temperature remains at 94°C, theory predicts that water vapor will condense at the reaction solution meniscus. Experimental results show the same trend as the theory but the experimental fluxes are positive for all temperature points tested. This difference could be due to the assumption in the simulations –fixed reaction solution meniscus position – that does not match the real reaction conditions. Moreover, the reaction solution meniscus may be heated above 94°C due to thermal crosstalk from the heated (*i.e.*, above 95°C) water meniscus, a situation that can be eliminated with proper device design. On-chip PCR with different water-meniscus operating temperatures produced similar amplification efficiency to off-chip positive controls (data not shown). In addition, similar to the results obtained in the thermally isolated device, no byproducts have been detected, and less evaporative loss also leads to higher amplification yield.

Design factors such as the geometry and location of the liquid stop play an important role in minimizing the vapor flux and the evaporative loss. As shown in Figure 7(a), the total vapor flux from the reaction solution meniscus decreases with decreasing liquid stop length. A shorter liquid stop reduces the distance between the vapor source (the pinned water meniscus) and the T-junction in the diffusion channel, thus increasing the vapor concentration at the T-junction. This increase will decrease the vapor concentration gradient between the reaction solution meniscus and the T-junction, resulting in less vapor flux from the reaction solution. A wider liquid stop (*i.e.*, a larger surface area of the pinned water meniscus) also facilitates the reduction of vapor flux from the reaction solution by increasing the vapor concentration at the T-junction (Figure 7(b)). Moreover, the lowest total flux from the reaction solution is achieved when the liquid stop intersects the diffusion channel at the midpoint (Figure 7(c)).

Conclusion

We have developed valveless strategies to reduce the sample evaporative loss during microfluidic thermal reactions using the principle of diffusion-limited evaporation. The microchannels on both sides of the reaction region provide long narrow diffusion paths that reduce the evaporation rate. Decreasing the driving force for evaporation by either increasing the thermal isolation of the reaction chamber or by increasing the concentration of water vapor in the diffusion channel will also limit the evaporation. Both theoretical and experimental results demonstrate that the proposed strategies can effectively reduce the evaporation rate during thermocycling and successfully perform PCR without using microvalves. Although PCR has been taken as an example to demonstrate the capability of the devices, the novel

miniaturized methodologies provided by these devices can also be applied in microfluidic devices for other chemical and biochemical reactions. Moreover, these methodologies can be readily integrated into more advanced devices such as integrated analysis systems.

Supplementary Material

Refer to Web version on PubMed Central for supplementary material.

Acknowledgments

The authors would like to gratefully acknowledge the funding of this work through several grants from NHGRI (most recently P01-HG001984) and a grant from NIAID (R01-AI049541) at the National Institutes of Health. The authors would like to acknowledge Brian N. Johnson, Rohit Pal, Nimisha Srivastava, Dylan Heldsinger, Kenneth J. Chomistek, S. Zafar Razzacki, Kenneth Alfano, Zheng Chen, Prasanna Thwar, Kyung Eun Sung, Onnop Srivannavit, Zhishan Hua, Sang-Hyun Lee and Myung-Gyu Kang for their assistance with reagent preparation, device fabrication, computer programming, SEM imaging, lab maintenance, electronic interface development and general discussion.

References

1. Sanger F, Nicklen S, Coulson AR. Proc Natl Acad Sci USA 1977;74:5463. [PubMed: 271968]
2. Barany F. Proc Natl Acad Sci USA 1991;88:189. [PubMed: 1986365]
3. Woolley AT, Hadley D, Landre P, DeMello AJ, Mathies RA, Northrup MA. Anal Chem 1996;68:4081. [PubMed: 8946790]
4. Waters LC, Jacobson SC, Kroutchinina N, Khandurina J, Foote RS, Ramsey JM. Anal Chem 1998;70:158. [PubMed: 9463271]
5. Waters LC, Jacobson SC, Kroutchinina N, Khandurina J, Foote RS, Ramsey JM. Anal Chem 1998;70:5172. [PubMed: 9868915]
6. Khandurina J, Mcknight TE, Jacobson SC, Waters LC, Foote RS, Ramsey JM. Anal Chem 2000;72:2995. [PubMed: 10905340]
7. Anderson RC, Su X, Bogdan GJ, Fenton J. Nucleic Acids Res 2000;28:e60. [PubMed: 10871383]
8. Lagally ET, Simpson PC, Mathies RA. Sensor Actuat B 2000;63:138.
9. Lagally ET, Medintz I, Mathies RA. Anal Chem 2001;73:565F. [PubMed: 11217764]
10. Hong JW, Fujii T, Seki M, Yamamoto T, Endo I. Electrophoresis 2001;22:328. [PubMed: 11288901]
11. Yuen PK, Kricka LJ, Fortina P, Panaro NJ, Sakazume T, Wilding P. Genome Res 2001;11:405. [PubMed: 11230164]
12. Liu Y, Rauch CB, Stevens RL, Lenigk R, Yang J, Rhine DB, Grodzinski P. Anal Chem 2002;74:3063. [PubMed: 12141665]
13. Shin YS, Cho K, Lim SH, Chung S, Park SJ, Chung C, Han DC, Chang JK. J Micromech Microeng 2003;13:768.
14. Fu LM, Lin CH. Biomed Microdevices 2007;9:277. [PubMed: 17195107]
15. Blazej RG, Kumaresan P, Mathies RA. Proc Natl Acad Sci USA 2006;103:7240. [PubMed: 16648246]
16. Cheng J, Shoffner MA, Mitchelson KR, Kricka LJ, Wilding P. J Chromatogr A 1996;732:151. [PubMed: 8646332]
17. Lagally ET, Emrich CA, Mathies RA. Lab Chip 2001;1:102. [PubMed: 15100868]
18. Lagally ET, Scherer JR, Blazej RG, Toriello NM, Diep BA, Ramchandani M, Sensabaugh GF, Riley LW, Mathies RA. Anal Chem 2004;76:3162. [PubMed: 15167797]
19. Koh CG, Tan W, Zhao MQ, Ricco AJ, Fan ZH. Anal Chem 2003;75:4591. [PubMed: 14632069]
20. Liu RH, Yang JN, Lenigk R, Bonanno J, Grodzinski P. Anal Chem 2004;76:1824. [PubMed: 15053639]
21. Yoon DS, Lee YS, Lee Y, Cho HJ, Sung SW, Oh KW, Cha J, Lim G. J Micromech Microeng 2002;12:813.
22. Zhao Z, Cui Z, Cui D, Xia S. Sensor Actuat A 2003;108:162.

23. Rodriguez I, Lesaicherre M, Tie Y, Zou Q, Yu C, Singh J, Meng LT, Uppili S, Li SFY, Gopalakrishnakone P, Selvanayagam ZE. Electrophoresis 2003;24:172. [PubMed: 12652588]
24. Wang H, Chen J, Zhu L, Shadpour H, Hupert ML, Soper SA. Anal Chem 2006;78:6223. [PubMed: 16944905]
25. Hashimoto M, Hupert ML, Murphy MC, Soper SA. Anal Chem 2005;77:3243. [PubMed: 15889915]
26. Lee DS, Park SH, Yang H, Chung KH, Yoon TH, Kim SJ, Kim K, Kim YT. Lab Chip 2004;4:401. [PubMed: 15269812]
27. Kopp MU, De Mello AJ, Manz A. Science 1998;280:1046. [PubMed: 9582111]
28. Obeid PJ, Christopoulos TK, Crabtree HJ, Backhouse CJ. Anal Chem 2003;75:288. [PubMed: 12553764]
29. Park N, Kim S, Hahn JH. Anal Chem 2003;75:6029. [PubMed: 14588047]
30. Hashimoto M, Chen PC, Mitchell MW, Nikitopoulos DE, Soper SA, Murphy MC. Lab Chip 2004;4:638. [PubMed: 15570378]
31. Liu J, Enzelberger M, Quake S. Electrophoresis 2002;23:1531. [PubMed: 12116165]
32. Oda RP, Strausbauch MA, Huhmer AFR, Borson N, Jurrens SR, Craighead J, Wettstein PJ, Eckloff B, Kline B, Landers JP. Anal Chem 1998;70:4361. [PubMed: 9796420]
33. Huhmer AFR, Landers JP. Anal Chem 2000;72:5507. [PubMed: 11080907]
34. Giordano BC, Ferrance J, Swedberg S, Huhmer AFR, Landers JP. Anal Biochem 2001;291:124. [PubMed: 11262165]
35. Chen J, Wabuyele M, Chen H, Patterson D, Hupert M, Shadpour H, Nikitopoulos D, Soper SA. Anal Chem 2005;77:658. [PubMed: 15649068]
36. Pollack MG, Paik PY, Shenderov AD, Pamula VK, Dietrich FS, Fair RB. μTAS 2003:619.
37. Krishnan M, Ugaz VM, Burns MA. Science 2002;298:793. [PubMed: 12399582]
38. Wheeler EK, Benett W, Stratton P, Richards J, Chen A, Christian A, Ness KD, Ortega J, Li LG, Weisgraber TH, Goodson K, Milanovich F. Anal Chem 2004;76:4011. [PubMed: 15253636]
39. Pal R, Yang M, Lin R, Johnson BN, Srivastava N, Razzacki SZ, Chomistek KJ, Heldsinger D, Haque RM, Ugaz VM, Thwar P, Chen Z, Alfano K, Yim M, Krishnan M, Fuller AO, Larson RG, Burke DT, Burns MA. Lab Chip 2005;5:1024. [PubMed: 16175256]
40. Yuen PK, Kricka LJ, Wilding P. J Micromech Microeng 2000;10:401.
41. Grover WH, Skelley AM, Liu CN, Lagally ET, Mathies RA. Sensor Actuat B-Chem 2003;89:315.
42. Thorsen T, Maerkl SJ, Quake SR. Science 2002;298:580. [PubMed: 12351675]
43. Liu J, Hansen C, Quake SR. Anal Chem 2003;75:4718. [PubMed: 14674446]
44. Pal R, Yang M, Johnson BN, Burke DT, Burns MA. Anal Chem 2004;76:3740. [PubMed: 15228349]
45. Perry, RH.; Green, DW. Perry's Chemical Engineers' Handbook. Vol. 7. 1997. p. 2-49.
46. Geankoplis, CJ. Transport Processes and Unit Operations. Vol. 3. 1993. p. 396
47. Yang M, Pal R, Burns MA. J Micromech Microeng 2005;15:221.
48. Jin S, Breuer KS. IMECE 2003:44135.
49. Man, PF.; Mastrangelo, CH.; Burns, MA.; Burke, DT. MEMS '98. Heidelberg, Germany: 1998. p. 45-50.

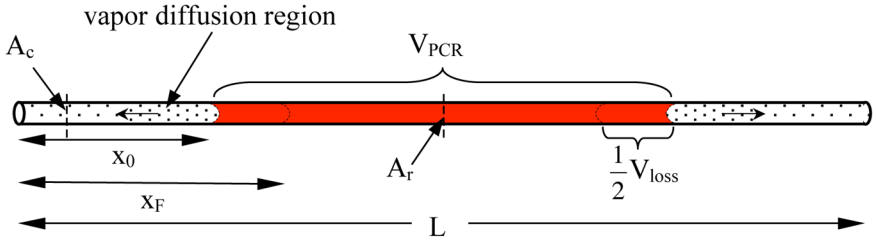

(a)

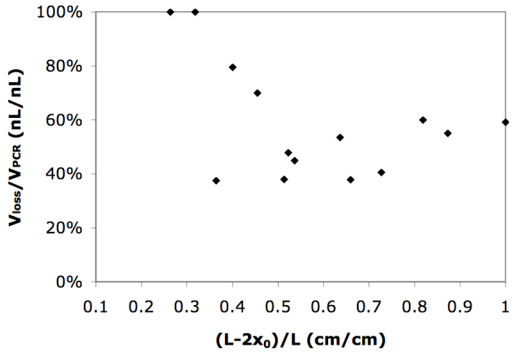

(b)

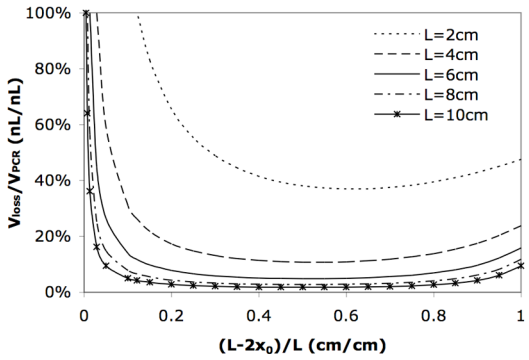

(c)

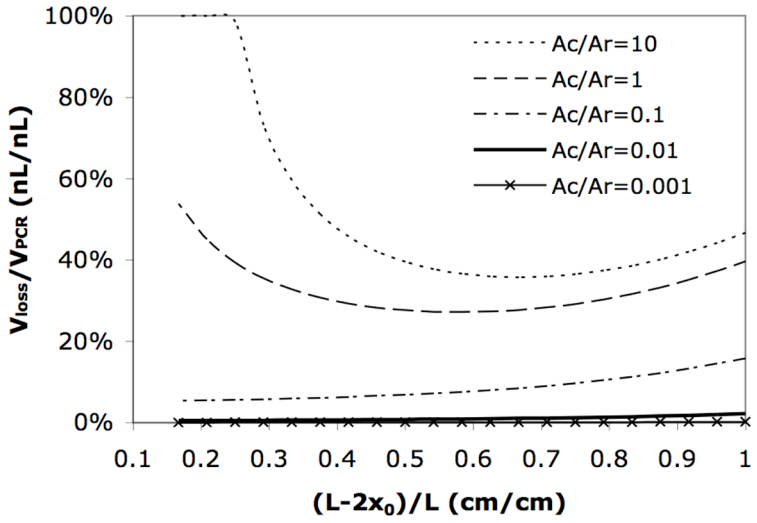

(d)

Figure 1.

(a) Schematic of the simple reactor. x_0 is the initial diffusion length; x_F is the final diffusion length; A_c is the cross-section area of the diffusion path; A_r is the cross-section area of the reaction region; L is the total length of the channel. (b) Experimental relative evaporative loss V_{loss}/V_{PCR} in a 2cm straight uniform channel with varying fractional filled length $(L - 2\ x_0)/L$. (c) Calculated relative evaporative loss V_{loss}/V_{PCR} in a straight uniform channel with different channel length. (d) Calculated relative evaporative loss V_{loss}/V_{PCR} in a channel-chamber-channel design with different cross-section area ratio A_c/A_r. The total length of the channels and chamber is 2.4cm and the reaction chamber is 0.4cm long.

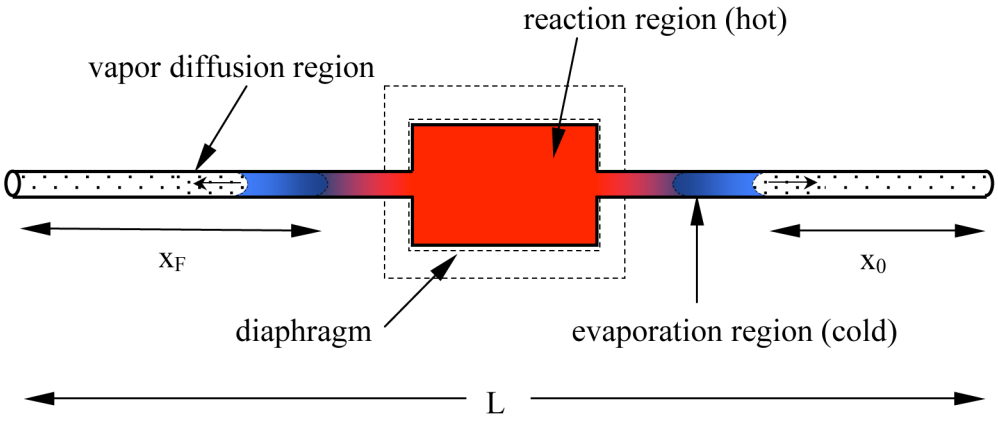

(a)

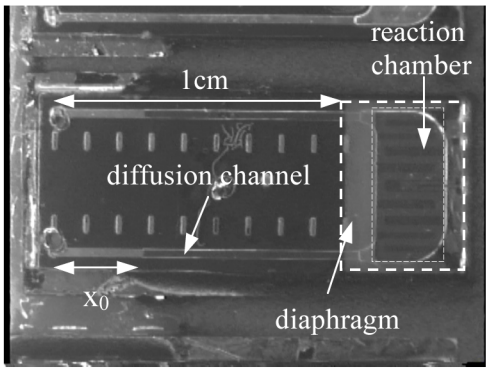

(b)

Figure 2.

(a) Schematic of the long-armed device with thermal isolation. The color gradient conceptually represents the temperature gradient. The actual temperature gradient is shown in Figure 1(e)–(g) in ESI. (b) Picture of the microfabricated device.

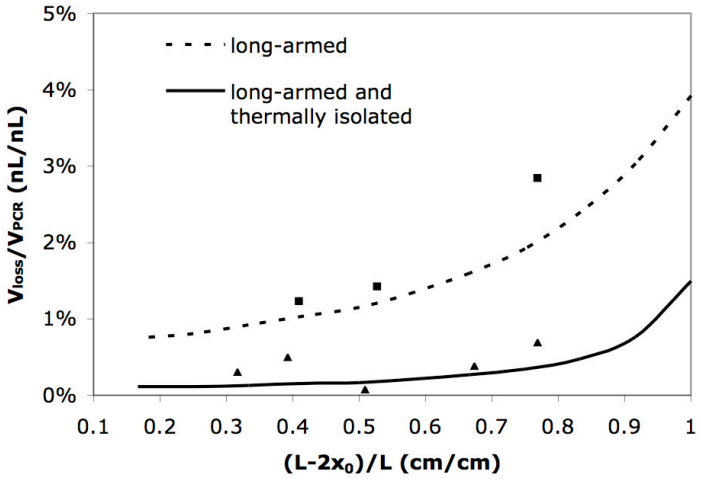

(a)

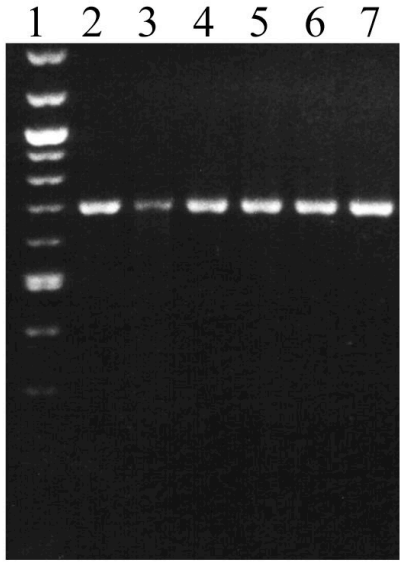

(b)

Figure 3.

(a) Calculated and experimental relative evaporative loss V_{loss}/V_{PCR} as a function of the fractional filled length $(L-2x_0)/L$. The cross-section areas of reaction chamber A_r and diffusion channel A_c used in the calculation and experiment are 0.2mm^2 and 0.004mm^2, respectively. ■ experimental data in a long-armed device without thermal isolation; ▲ experimental data in a long-armed device with thermal isolation. (b) Gel electrophoresis of PCR products in the long-armed device with thermal isolation. Lane 1, the 100bp DNA ladder. Lane 2-lane 6, on-chip PCR products. The extra sample volumes in the channels are 7.2%, 6.1%, 4.1%, 2.7% and 1.8% of the reaction volume, respectively. The corresponding values of relative evaporative loss and fractional filled length refer to the experimental data points (from right to left) shown

in (a). Lane 7, a positive PCR control carried out in a commercial thermocycler. Lane 3 exhibits lower fluorescent intensity due to sample volume loss during the sample collection process.

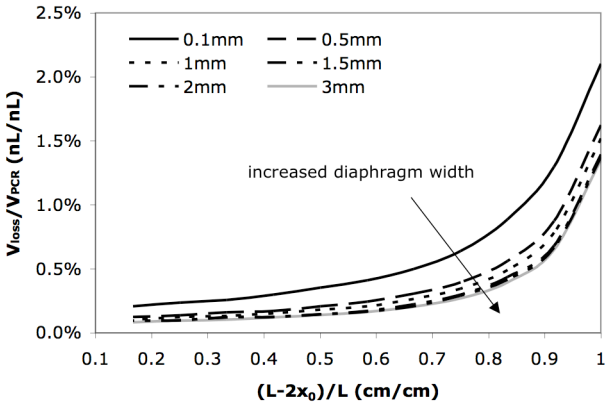

(a)

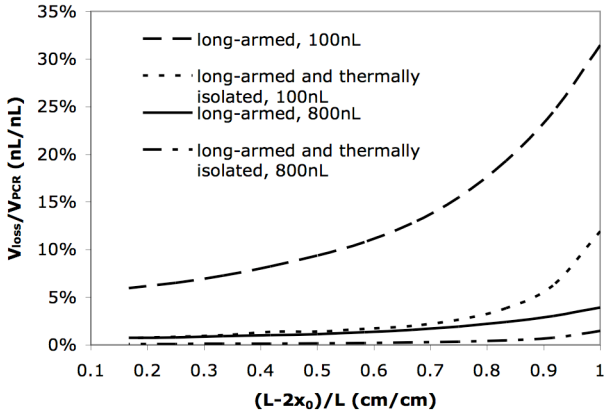

(b)

Figure 4.

(a) The relative evaporative loss in a thermally isolated long-armed device with different diaphragm width. (b) The relative evaporative loss V_{loss}/V_{PCR} for different reaction volume in a long-armed device with and without thermal isolation.

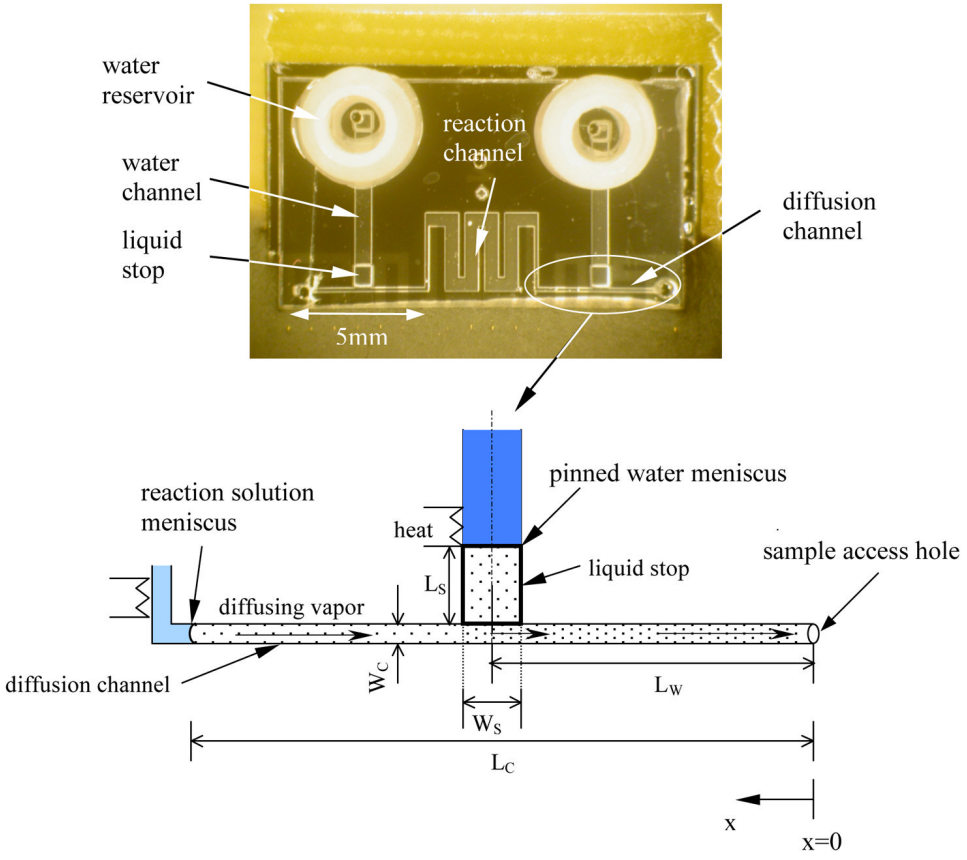

Figure 5.

(a) Picture of the device with vapor replenishment. L_w is the distance from the sample access hole to the centerline of liquid stop; L_c is the distance from the sample access hole to the reaction solution meniscus; W_c is the width of the diffusion channel; L_s and W_s are the length and width of the liquid stop, respectively. (b) A SEM image of the liquid stop structure.

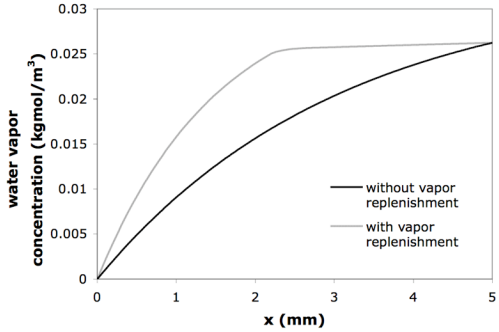

(a)

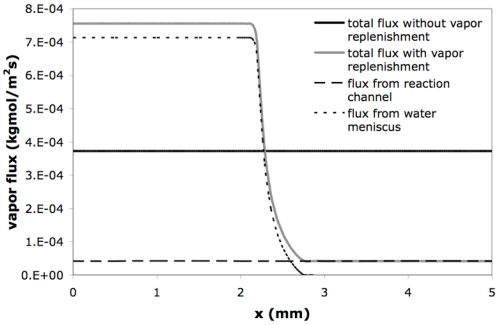

(b)

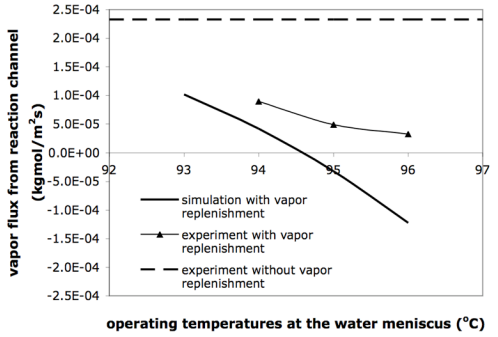

(c)

Figure 6.

(a) Vapor concentration and (b) vapor flux along the centerline of the diffusion channel in the simulation results. L_c = 5mm; W_c = 100μm; L_s =1mm; W_s = 0.6mm. L_c, W_c, L_s and W_s are defined in the captions of Figure 5(a). (c) Vapor flux from the reaction channel with different operating temperatures at the pinned water meniscuses. Note that a positive flux represents an inbound flux (toward the sample access hole) while a negative flux represents an outbound flux (toward the reaction solution meniscus).

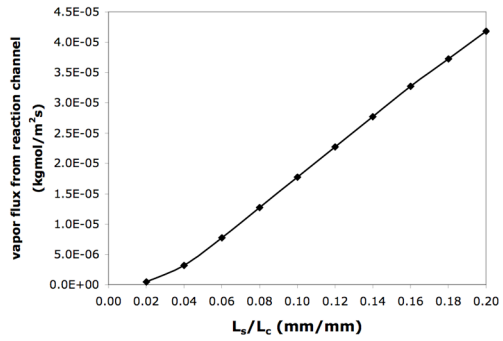

(a)

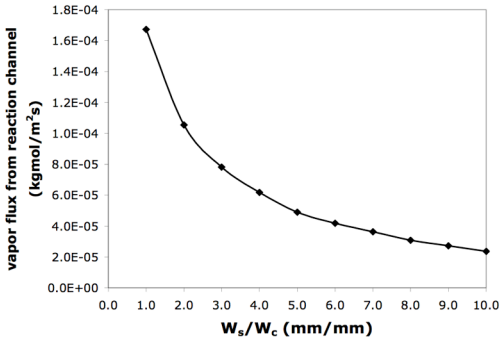

(b)

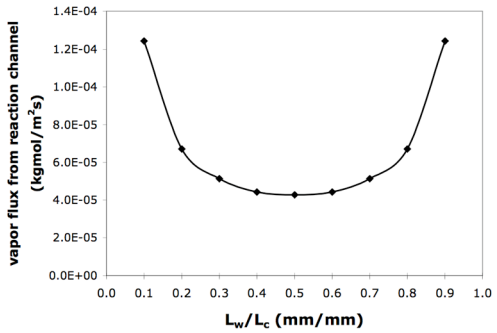

(c)

Figure 7.

Simulation results of vapor fluxes from the reaction channel (a) when different length of the liquid stop is used; (b) when different width of the liquid stop is used; (c) when the location of the liquid stop varies with L_S =1mm and W_S = 0.6mm. All the simulations use 94°C as the operating temperature at the water meniscus, L_C = 5mm and W_C = 100μm. L_C, W_C, L_W, L_S and W_S are defined in the caption of Figure 5(a).

Table 1

Interfacial temperature, vapor pressure, vapor diffusivity and reaction time used in the calculations

PCR steps	variables	uniform straight channel	long-armed device without thermal isolation	long-armed device with thermal isolation
denaturation	T_{i1}	367K (94°C)	360 K (87°C)	313 K(40°C)
	P_{v1}	81447 Pa	62660 Pa	7375 Pa
	D_{v1}	3.62×10^{-5} m^2/s	3.50×10^{-5} m^2/s	2.74×10^{-5} m^2/s
	t_{F1}	5 s	5 s	5 s
annealing	T_{i2}	328K (55°C)	325 K (52°C)	303 K (30°C)
	P_{v2}	15737 Pa	14000 Pa	4240 Pa
	D_{V2}	2.97×10^{-5} m^2/s	2.92×10^{-5} m^2/s	2.59×10^{-5} m^2/s
	t_{F2}	10 s	10 s	10 s
extension	T_{i3}	345K (72°C)	340 K (67°C)	308 K (35°C)
	Pv_3	33944 Pa	28000 Pa	5626 Pa
	D_{v3}	3.25×10^{-5} m^2/s	3.16×10^{-5} m^2/s	2.66×10^{-5} m^2/s
	t_{F3}	20 s	20 s	20 s